

## Inversion for refractivity parameters from radar sea clutter

Peter Gerstoft,<sup>1</sup> L. Ted Rogers,<sup>2</sup> Jeffrey L. Krolik,<sup>3</sup> and William S. Hodgkiss<sup>1</sup>

Received 5 March 2002; revised 31 May 2002; accepted 10 July 2002; published 4 April 2003.

[1] This paper describes estimation of low-altitude atmospheric refractivity from radar sea clutter observations. The vertical structure of the refractive environment is modeled using five parameters, and the horizontal structure is modeled using six parameters. The refractivity model is implemented with and without an a priori constraint on the duct strength, as might be derived from soundings or numerical weather-prediction models. An electromagnetic propagation model maps the refractivity structure into a replica field. Replica fields are compared to the observed clutter using a squared-error objective function. A global search for the 11 environmental parameters is performed using genetic algorithms. The inversion algorithm is implemented on S-band radar sea-clutter data from Wallops Island, Virginia. Reference data are from range-dependent refractivity profiles obtained with a helicopter. The inversion is assessed (1) by comparing the propagation predicted from the radar-inferred refractivity profiles and from the helicopter profiles, (2) by comparing the refractivity parameters from the helicopter soundings to those estimated, and (3) by examining the fit between observed clutter and optimal replica field. This technique could provide near-real-time estimation of ducting effects. In practical implementations it is unlikely that range-dependent soundings would be available. A single sounding is used for evaluating the radar-inferred environmental parameters. When the unconstrained environmental model is used, the “refractivity-from-clutter,” the propagation loss generated and the loss from this single sounding, is close within the duct; however, above the duct they differ. Use of the constraint on the duct strength leads to a better match also above the duct. *INDEX TERMS:* 3360 Meteorology and Atmospheric Dynamics: Remote sensing; 6904 Radio Science: Atmospheric propagation; 6969 Radio Science: Remote sensing; 6982 Radio Science: Tomography and imaging; *KEYWORDS:* atmospheric refractivity estimation, radar clutter, genetic algorithms, radar cross section

**Citation:** Gerstoft, P., L. T. Rogers, J. L. Krolik, and W. S. Hodgkiss, Inversion for refractivity parameters from radar sea clutter, *Radio Sci.*, 38(3), 8053, doi:10.1029/2002RS002640, 2003.

### 1. Introduction

[2] Two common refractivity structures that significantly affect the performance of shipboard radars are evaporation ducts and surface-based ducts (see Figure 1). When a duct is present the low altitude propagation loss will usually be much less than for a standard atmosphere,

and thus increasing the range at which low-altitude targets can be detected.

[3] Surface-based ducts appear about 15% of the time worldwide, 25% of the time off Southern California Coast, and 50% of the time in the Persian Gulf [Patterson, 1992]. While surface-based ducts are less common than evaporation ducts, their effects frequently are more dramatic. They often manifest themselves in a radar's plan position indicator (PPI) as clutter rings, see Figure 2 (the SPANDAR radar is described in section 2), and they can result in significant height errors for 3-D radar as the lowest elevation scans become trapped on the surface instead of refracting upward as would be expected for a standard atmosphere. Many efforts in remote sensing and numerical weather prediction have been directed at better estimation of the refractivity structure in the lowest 1000 m above the sea surface [see Richter, 1995; Rogers, 1997]. Alternatives for estimating the refractivity struc-

<sup>1</sup>Marine Physical Laboratory, University of California, San Diego, La Jolla, California, USA.

<sup>2</sup>Atmospheric Propagation Branch, Space and Naval Warfare Systems Command Systems Center, San Diego, California, USA.

<sup>3</sup>Department of Electrical and Computer Engineering, Duke University, Durham, North Carolina, USA.

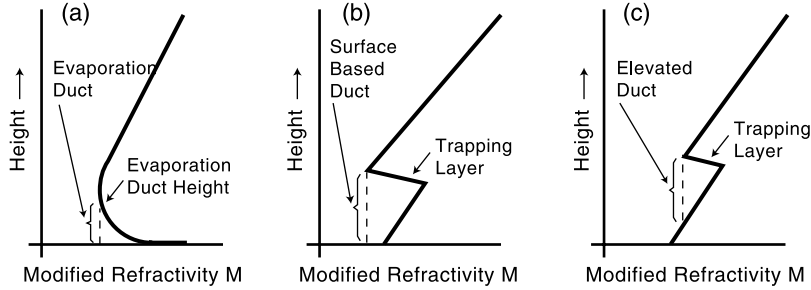


**Figure 1.** Modified refractivity  $M$  versus height. (a) Evaporation duct (typical height 0–30 m); (b) surface-based duct (typical height 30–1000 m); (c) elevated duct. The modified refractivity is the refractivity multiplied with  $10^6$  and corrected for the curvature of Earth.

ture that is not associated with the surface layer are in situ sampling via radiosondes or rocketsondes [Rowland et al., 1996], or through numerical weather prediction models [see Haack and Burk, 2001].

[4] Because the effects of surface-based ducting are visibly manifested in radar clutter, it might be feasible to extract information about the duct's refractive structure from the clutter. Such a “refractivity-from-clutter” (RFC) capability might provide near-real-time, azimuth-dependent information about the ducting conditions, as opposed

to current practice where the characterization is based only on the ship-launched in situ instrument, whose time-lateness is from tens of minutes to several hours. Furthermore, RFC might require no emissions beyond those inherent in the operation of the ship's radar, nor would RFC require additional deck-mounted equipment; these are critical considerations.

[5] Inferring refractivity parameters from observations of radar clutter is an inverse problem. The Bayesian framework for solving for solving such problems is laid

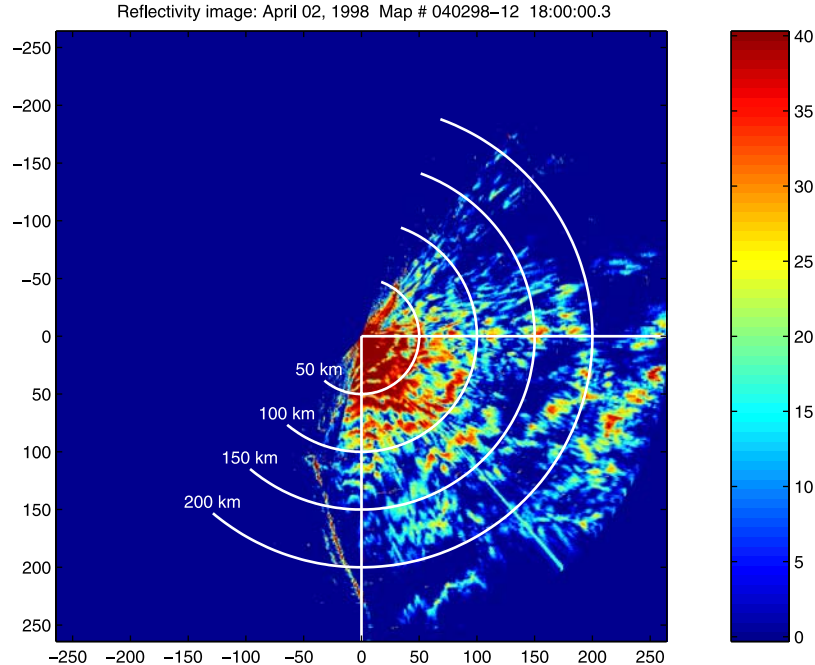


**Figure 2.** Reflectivity map (dBZ) from SPANDAR corresponding to Wallops run 12 (time 13:00EST, see also section 2). The elevation angle is  $0^\circ$  and horizontal and vertical range are in kilometers.

out by *Tarantola* [1987]. Within the Bayesian framework, the general steps involved in RFC for surface-based ducts are as follows:

[6] 1. The input data is a vector of received clutter power values  $\mathbf{P}_c^{\text{obs}}$  at discrete ranges  $r_1, r_2, \dots, r_N$ .

[7] 2. An environmental model  $\mathbf{H}_{\text{env}}$  maps an environmental parameter vector  $\mathbf{m}$  into  $\mathbf{M}$ , a vector or matrix of values of modified refractivity  $M$  over the discrete ranges and heights of interest.

[8] 3. A combined electromagnetic (EM) propagation model (we use TPEM [*Barrios*, 1994]) and radar model  $\mathbf{H}_{\text{prop}}$  maps  $\mathbf{M}$  into a replica field  $\mathbf{P}_c(\mathbf{m}) = \mathbf{H}_{\text{prop}}(\mathbf{H}_{\text{env}}(\mathbf{m}))$ .

[9] 4. An objective function  $f$  calculates the fit of  $\mathbf{P}_c(\mathbf{m})$  to  $\mathbf{P}_c^{\text{obs}}$ .

[10] 5. A global optimization procedure is used search over all  $\mathbf{m}$  to find the optimal value  $\hat{\mathbf{m}}$  of the  $f(\mathbf{P}_c^{\text{obs}}, \mathbf{P}_c(\mathbf{m}))$ .

[11] 6. An assessment is made of the quality of the solution by examining forward model solutions or parameter error estimates/distributions [see, e.g., *Gerstoft and Mecklenbräuker*, 1998]. This is important as a global solution always will provide an estimate, and, for example, it could indicate that a wrong environmental model is used. For convenience, we refer to this as a “global parameter” algorithm since each new combination of the elements of  $\mathbf{m}$  requires a new run of the forward model.

[12] The inference of refractivity parameters associated with surface-based ducts was first posed by *Krolik and Tabrikian* [1998] as a maximum a posteriori (MAP) estimation problem. In that initial work, the environmental parameter vector  $\mathbf{m}$  had only three elements: two to describe the vertical structure of refractivity and one to describe the range dependency of the environment. The algorithm worked well in some instances; however, often the optimal replica field did not match the observed data. This phenomenon could be attribute to the horizontal variability of the sea clutter radar cross section  $\sigma^o$ . It is more likely, however, that the dominant problem was having too simple a model for the refractive environment, one that could not account for variations that resulted in horizontal shifting of features. Note, however, that while the horizontal variability of  $\sigma^o$  probably is not the cause of poor fits, it can have unwanted effects on inversion results and will be examined in section 5.3.

[13] The need for greater fidelity in modeling the refractive environment is being addressed by two groups using different methods. Krolik and coworkers are pursuing the development of a marching algorithm where the parameters describing the refractivity are updated at each range step of the parabolic equation and the environmental parameters are assumed to vary as a Markov process with respect to range. The latest results using the marching algorithm [*Anderson et al.*, 2001] are comparable to the results that presented here.

[14] This paper focuses on using a global-parameters approach with parameterizations of both vertical and horizontal structure of the refractive environment. This, then, is a multi-parameter optimization problem that is solved using a genetic algorithm search strategy [*Gerstoft*, 1994]. How the global parameter approach is realized reflects the varying degrees of maturity of the individual components:

[15] 1. There is no clearly identified “best” choice for  $\mathbf{H}_{\text{env}}$ ; the map from  $\mathbf{m}$  to  $\mathbf{P}_c(\mathbf{m})$  is always nonlinear as  $\mathbf{H}_{\text{prop}}$  is nonlinear. That precludes the use of tools such as Karhunen-Loeve for identifying principal components. In general, we expect that adding more parameters  $\mathbf{m}$  usually will result in a better match to  $\mathbf{P}_c^{\text{obs}}$ . But, if neither  $\mathbf{H}_{\text{env}}$  nor additional a priori restrictions on  $\mathbf{m}$  constrain the solution, then unrealistic values may be estimated. Additionally, adding more parameters increases the size of the search space. Thus developing  $\mathbf{H}_{\text{env}}$  is a balance between minimizing the number of parameters (to minimize the size of the search space) and having sufficient parameters so that close fits to  $\mathbf{P}_c^{\text{obs}}$  can be obtained, while constraining the solutions such that  $\mathbf{M} = \mathbf{H}_{\text{env}}(\mathbf{m})$  is restricted to realizations that are consistent with refractivity structures observed in nature.

[16] 2. The EM propagation models available for computing  $\mathbf{H}_{\text{prop}}$  are reasonably mature [*Levy*, 2000; *Dockery*, 1998] as is the modeling of the radar system.

[17] 3. The modeling of the sea-clutter radar cross section  $\sigma^o$  as a function of environmental parameters and its sensitivity to the grazing angle  $\psi$  is somewhat less mature and is discussed further in section 3.5. We handle the uncertainty in the modeling of sea clutter by making our objective function insensitive to the average value of  $\sigma^o$ , and thus freeing us of the need for rigorous modeling of the same. At the same time, the first range at which we use the clutter data is sufficiently distant from the radar to preclude the use of data where large grazing angles are present.

[18] 4. The objective function  $f$  is ideally determined from knowledge of errors in the forward modeling and the data. The  $f$  we choose is optimal for the case where the mismatch between  $\mathbf{P}_c(\hat{\mathbf{m}})$  and  $\mathbf{P}_c^{\text{obs}}$  is an independent, univariate, Gaussian process. However, it is expected to work well for cases where this is not satisfied.

[19] The remainder of this paper reports on the implementation of the global algorithm and is organized as follows: Radar observations and in situ validation data for a ducting event in the vicinity of Wallops Island, VA, on 2 April 1998, are described in section 2. Section 3 describes the forward modeling with an emphasis on the environmental modeling. The effects of the variability of the refractive environment on the clutter returns are illustrated in section 4. The results of implementing the inversion procedure using the above data are given in section 5.

**Table 1.** Space Range Radar (SPANDAR) Parameters for 2 April 1998 Observations

Parameter	Measurement
Frequency, GHz	2.84
Power, dBm	91.40
Beamwidth, deg	0.39
Antenna gain, dB	52.80
Height, m, MSL	30.78
Polarization	VV
Range bin width, m	600

[20] The results presented here are for cases where (1) the general nature of the cases considered (a duct created by the flow of warm, dry, continental air over a relatively colder ocean) vary little from case to case in comparison to the variations in ducting structures that would be encountered in a world-wide sampling, and (2) evidence points to the sea clutter radar cross section having little horizontal variability for the cases considered, whereas greater variability is likely to be encountered in a world

wide sampling. Testing over a wide range of data cases, as well as making the algorithm robust in the presence of a range-varying  $\sigma^0$ , and the use of prior knowledge of  $\sigma^0$  range dependency are necessary future steps.

## 2. Radar and Validation Data

[21] Radar and in situ validation data were obtained during the Wallops '98 measurement campaign [Rogers et al., 2000] conducted by the Naval Surface Warfare Center, Dahlgren Division. The data presented here are from the surface-based ducting event that occurred on 2 April 1998. Radar data were obtained using the Space Range Radar (SPANDAR) [Stahl and Crippen, 1994].

[22] The SPANDAR was originally designed as a tracking radar. It is equipped with (nominal) 4 MW and 1 MW transmitters and an 18.29-m parabolic antenna. Table 1 shows the radar's parameters as configured for the data taken here. Pulse widths (2  $\mu$ s) on the radar correspond to range-bin widths of 600 m. With 446 range bins available, this provides maximum range of

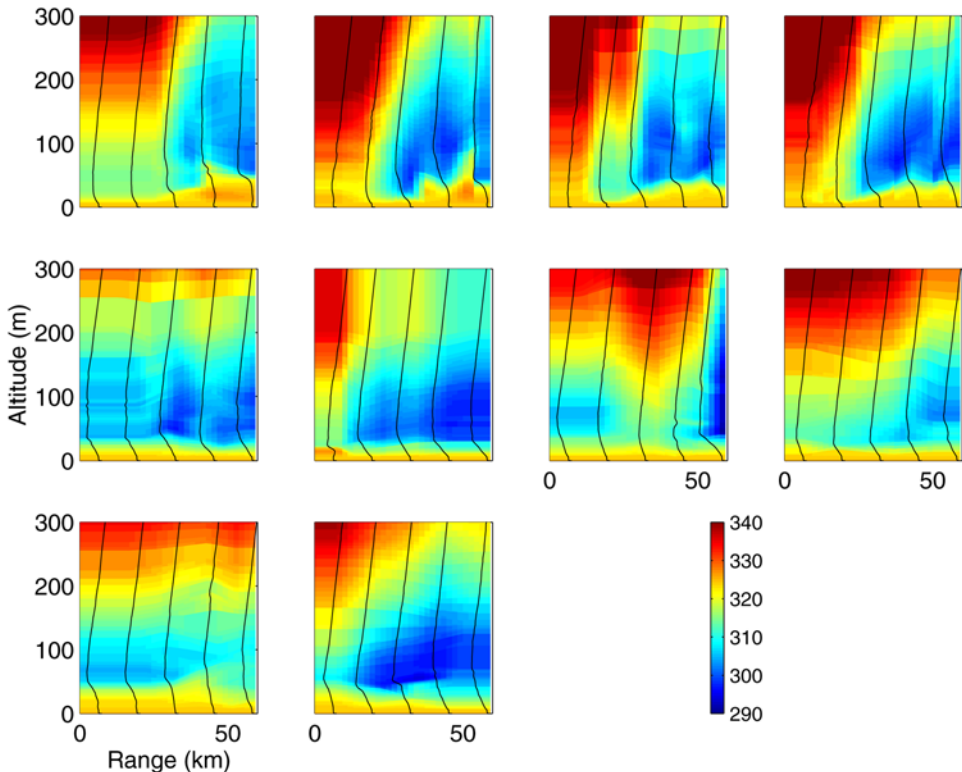


**Figure 3.** Modified refractivity profiles (M units) sequenced in time. The first row is observed from 8:47–10:26 EST (08:47–09:05, 09:07–09:32, 09:33–09:57, and 09:58–10:26), middle 12:26–14:15 EST (12:26–12:50, 12:52–13:17, 13:19–13:49, and 13:51–14:14), and bottom 16:00–16:52 EST (15:59–16:27 and 16:29–16:52). All refractivity profiles have been normalized to the same value (330 M units) at sea level.

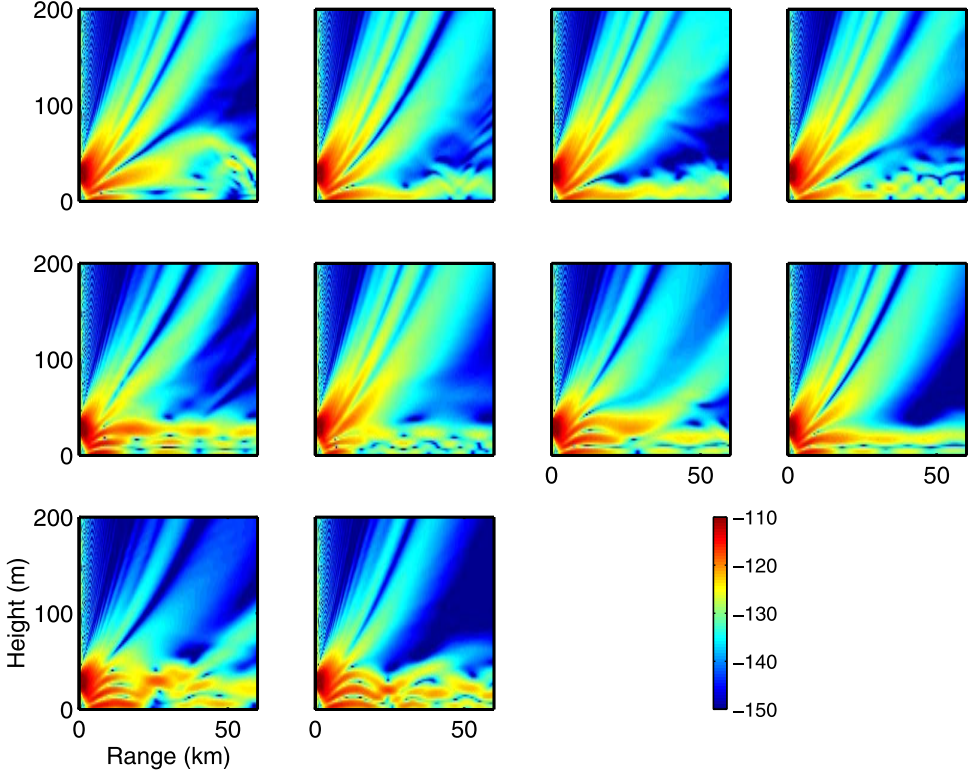


**Figure 4.** Coverage diagram (dB) for each of the refractivity profiles in Figure 3.

267 km, when the first range bin is set to 0 km. The radar is equipped with a Sigmet Radar Data System that provides reflectivity, velocity, time series, and spectra types of output. However, for the Wallops'98 experiment Signal-to-noise ratio (S/N) was recorded instead of reflectivity.

[23] A polar plot of S/N (or clutter map) at 0° elevation from a ducting event is shown in Figure 2. The edges around radials 30° and 180–200° are due to the coastline. The intensifications around ranges 130, 180, and 230 km are due to ducting propagation. To mitigate the effects point targets (including sea spikes), the radar data used in the inversions are median filtered across range (1.2 km, 3 samples) and azimuth (5°, 9 samples).

[24] Meteorological soundings were obtained by an instrumented helicopter provided by the Johns-Hopkins University Applied Physics Laboratory. The helicopter would fly in and out on the 150° radial from a point 4 km due east of the SPANDAR. During the flights, the helicopter would fly a saw-tooth up-and-down pattern and a single transect lasted about 30 min. Contour plots of modified refractivity versus range and height are shown in Figure 3. Dark lines superimposed on the plot are the modified refractivity profiles. The duct can be seen in the first 100 m. The figure illustrates the range

and time variability on the day of the experiment. The earlier profiles show substantial range dependency. This indicates that for inversion a range-dependent model might be needed.

[25] The refractivity profiles then were used to generate the corresponding coverage diagrams (Figure 4) using a parabolic equation propagation model, TPEM [Barrios, 1994]. The energy trapped in the duct (typically 0–50 m height) is clearly seen. It is observed that there are large differences between neighboring coverage diagrams. To quantify the change in neighboring coverage diagrams, following the procedure of Goldhirsh and Dockery [1998], the difference from one coverage diagram to the next is computed (Figure 5). Since  $10\log P_1 - 10\log P_2 = 10\log P_1/P_2$ , this corresponds to the ratio of the two fields expressed in dB. There is less difference between the fields within the duct compared to above the duct.

### 3. Forward Modeling and Inversion Algorithm

#### 3.1. Environmental Model $H_{env}$

[26] Surface-based ducts can be associated with either convective or stable boundary layers [see, e.g., Stull,

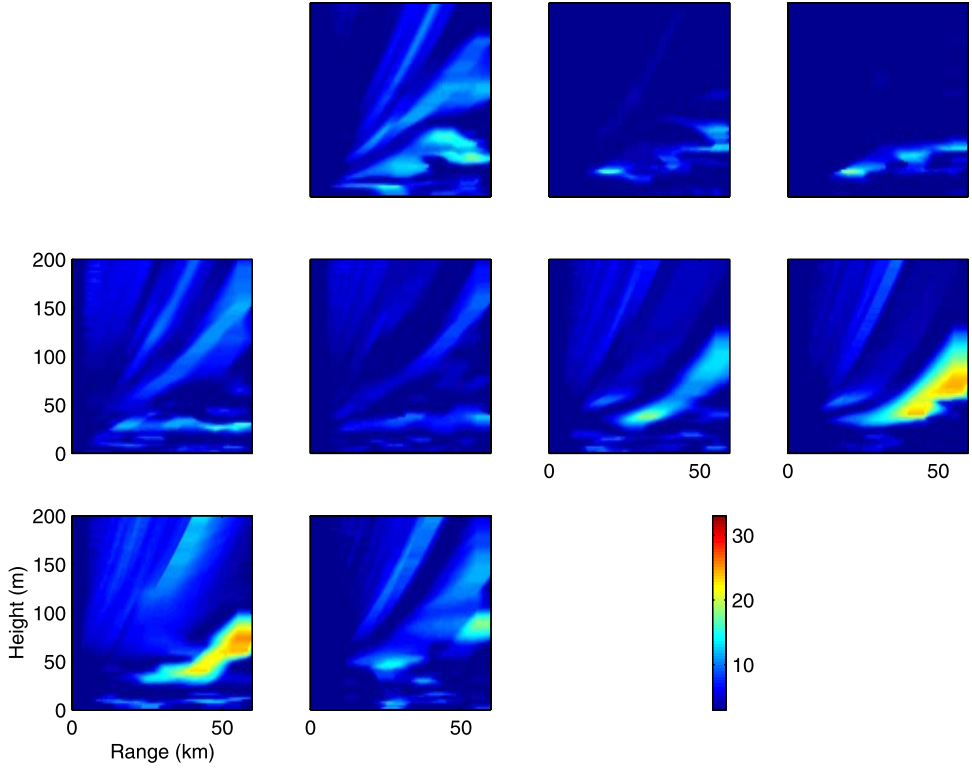


**Figure 5.** Relative change (dB) in fields between neighboring fields of Figure 4.

1998]. A typical case for the convective boundary layer is that the surface layer within the boundary layer is unstable (e.g.,  $T_{sea} > T_{air}$ ), and the vertical structure is described by Monin-Obukhov similarity theory. Above the surface layer is the mixed layer where the potential temperature and humidity are largely height-independent. It is shown by Gossard and Strauch [1983] that the gradient of modified refractivity  $dM/dz$  within the mixed layer will tend to a value of 0.13 M units/m. The capping inversion is the region between the mixed layer and the free troposphere and can have strongly negative modified refractivity gradients. Often the change in the gradient is quite pronounced, producing a “sharp top” that is discussed at length by Wyngaard *et al.* [2001].

[27] With the stable boundary layer, the surface layer is stable (e.g.,  $T_{sea} < T_{air}$ ), and the gradient of modified refractivity will transition from negative to positive values within distances ranging from a few to many tens of meters. There is no mixed layer or capping inversion per se, but as the profiles from the Wallops '98 experiment indicate (Figure 3), the profiles of modified refractivity can be quite complex.

[28] The environmental model illustrated in Figure 6 usually can describe refractivity profiles corresponding to either convective or stable cases. The model consists

of an evaporation duct profile (for the surface layer) and line segments corresponding to the mixed layer, capping inversion, and free troposphere for the case of a convective boundary layer. By letting the slope in the segment corresponding to the mixed layer take on negative values (as opposed to having a slope fixed at 0.13 M units/m), the model can also describe profiles associated with stable layers. However, when a stable layer is present then the mixed layer and inversion layer do not conform to the meteorological definition. The value of modified refractivity as a function of height is given by

$$M(z) = M_0 + \begin{cases} M_1 + c_0 \left( z - \delta \log \frac{z}{z_0} \right) & \text{for } z < z_d \\ c_1 z & \text{for } z_d < z < z_b \\ c_1 z_b - M_d \frac{z - z_b}{z_{\text{thick}}} & \text{for } z_b < z < z_t \\ c_1 z_b - M_d + c_2 (z - z_t) & \text{for } z_t < z, \end{cases} \quad (1)$$

where:

[29] 1. The expression  $c_0(z - \delta \log(\frac{z}{z_0}))$  with roughness factor  $z_0 = .00015$  and  $c_0 = 0.13$  corresponds to the

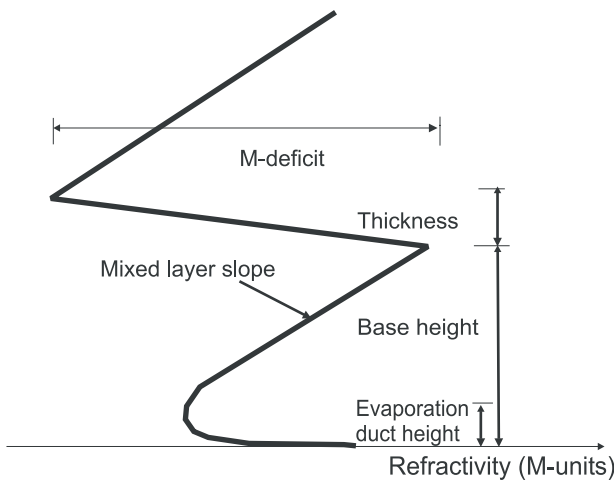


**Figure 6.** Five-parameter refractivity model.

neutral refractivity profile described by Paulus [1990].  $\delta$  is the evaporation duct height.

[30] 2.  $c_1$  is the slope in the mixed layer. A feasible range is  $[-1, 0.4]$  M units/m. This includes the typical value of 0.13 M units/m for a convective boundary layer [Gossard and Strauch, 1983].

[31] 3.  $c_2 = 0.118$  M units/m, which is consistent with the mean over the whole of the United States. Because the profiles are upward refracting, this is not a sensitive parameter.

[32] 4.  $z_d$  is determined by

$$z_d = \begin{cases} \frac{\delta}{1 - c_1/c_0} & \text{for } 0 < \frac{1}{1 - c_1/c_0} < 2 \\ 2\delta & \text{otherwise} \end{cases}, \quad (2)$$

subject to  $z_d < z_b$ . When  $z_d = 2\delta$  (the lower condition in equation (2)) the slope is not continuous.

[33] 5.  $z_b$  is the trapping-layer base height. We choose to allow it to vary from 0 to 500 m. When the base height is 0 m, a bilinear profile is obtained.

[34] 6.  $z_{\text{thick}}$  is thickness of the inversion layer. A typical range is  $[0, 100]$  m.

[35] 7.  $z_t$  is determined by

$$z_t = z_b + z_{\text{thick}}. \quad (3)$$

[36] 8.  $M_0 = 330$  M units is the offset of the M profile, determined as the value at which the mixed layer slope intersects  $z = 0$ . For the field calculated at a single frequency, the offset is not important and is chosen arbitrarily.

[37] 9.  $M_1$  is determined by

$$M_1 = c_0 \delta \log \frac{z_d}{z_0} + z_d(c_1 - c_0). \quad (4)$$

[38] 10.  $M_d$  is M deficit of the inversion layer. We allow it to vary from  $[0, 100]$  M units.

[39] It is clear that the helicopter profiles in Figure 3 show considerably horizontal variation. Although we are not (at least at this point) specifically interested in these variations, they lead to horizontal shifting of intensifications in the clutter (as will be illustrated in section 4), which may be realized in ways that might not be feasible for a horizontally homogeneous refractivity structure. Previous research (unpublished) demonstrated that such shifting is problematic for the squared-error objective function that is used in the inversions. One way of handling this “compliance” problem is to add degrees of freedom to the environmental model that describe horizontal variations in the refractivity structure.

[40] In section 4 it will be shown that over some neighborhood, a general shift in the location of intensifications in the clutter could be accounted for ambiguously by one or more of the parameters describing the vertical refractivity structure. Therefore it might be possible to obtain the desired compliance by allowing range dependency in just one of the parameters describing the vertical structure, particularly the trapping layer base height  $z_t$ . We choose to add compliance to the model by adding parameters that are coefficients corresponding to the principal components of modeling the behavior of  $z_t$  as a Markov process with respect to range.

[41] The principal components are determined using the Karhunen-Loeve method as follows (Figure 7). First,  $10^6$  Markov realizations of base height variation versus range were generated (Figure 7a). For each kilometer, the base height was updated using a Gaussian distribution with a standard deviation of 1 m (this is arbitrarily chosen since the process is linear, and it can be scaled later). Due to transition from land to sea, the profiles were referenced at 10 km so that they all had a value of 0 at range 10 km. Next, the main eigenvectors and eigenvalues were determined from the correlation matrix generated from the realizations of the base height. As an example, Figure 7a shows 20 realizations of the base-height from the Markov model. Subsequently, Figure 7d shows 20 realizations of base-height variation based on the first five eigenvectors, which capture the same general range dependency as illustrated in Figure 7a. For the environmental model, the weighting for each eigenvector is picked from a uniform distribution between plus/minus the square root of the eigenvalues. This effectively constrains the base height variations to  $\pm 50$  m over the range of 0 to 100 km, but allows substantial freedom within that range.

### 3.2. Search Bounds for Parameters

[42] The set of parameters described in section 3.1 was used in the optimization. The parameters and their search bounds are given in Table 2. For the base-height coef-

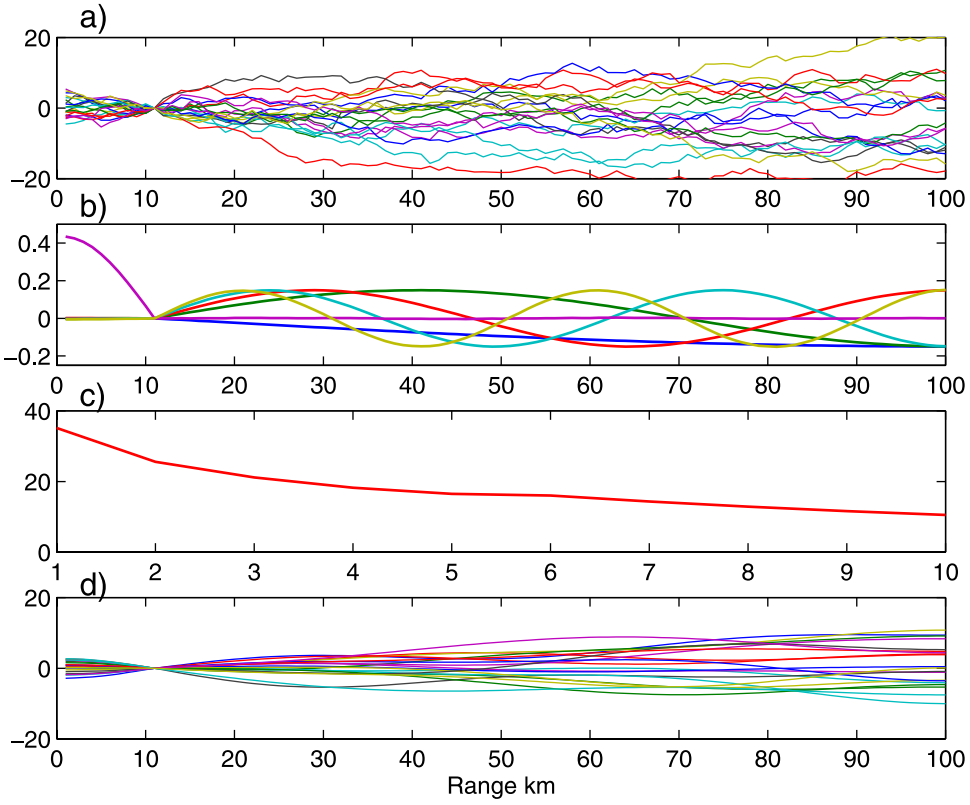


**Figure 7.** Model for range dependence of base height. (a) Twenty (out of  $10^6$ ) Markov realization of base height; (b) first 6 eigenvectors; (c) first 10 eigenvalues; and (d) 20 realizations based on first 5 eigenvectors.

ficient they were determined as plus/minus a fraction of the square root of the eigenvalues found in section 3.1.

[43] In actual implementations, prior information might be available from a variety of sources (e.g., numerical weather prediction models, atmospheric soundings, etc.) that could improve the quality of the inverse problem solutions. As an example, consider that a sounding is available from which we can diagnose the top of the trapping layer ( $z_{top}^{obs}$ ) and its associated value of modified refractivity. For a surface duct, this will correspond to the minimum value of the M profile. Assuming that the value of modified refractivity immediately above the sea surface remains constant, that the air mass above the top of the trapping layer remains constant in time, and that the lapse-rate for refractivity in that air mass is  $c_{lap}$  leads to the relationship

$$M(z_{top}) \approx M(z_{top}^{obs}) + (z_{top} - z_{top}^{obs}) * c_{lap} \quad (5)$$

for any value of  $z_{top}$ .  $c_{lap}$  is either taken as the slope for a convective boundary layer ( $c_1 = 0.118$  M units/m) or average slope above the trapping layer ( $c_2 = 0.118$  M units/m). It will be seen in section 5.2 that for the cases

considered here, the refractivity inversion algorithm tends to overestimate the degree of trapping. Examination of the soundings shown in Figure 3 and the use of (5) leads to the inequality constraint

$$M(z_{top}) - M(0) - c_{lap}z_{top} > -60 \quad (6)$$

that should serve to correct the described problem. In section 5.3, it is shown that implementation of equation

**Table 2.** Parameter Search Bounds for the Range-Dependent Model

Parameter	Lower Bound	Upper Bound
Thickness $z_{thick}$ , m	0	100
M deficit $M_d$ , M units	0	100
Mixed layer slope $c_1$ , M units/m	-1	0.4
Evaporation duct height $\delta$ , m	0	40
Base height offset, m	3	300
Base height coefficient 1	-570	570
Base height coefficient 2	-190	190
Base height coefficient 3	-110	110
Base height coefficient 4	-80	80
Base height coefficient 5	-65	65

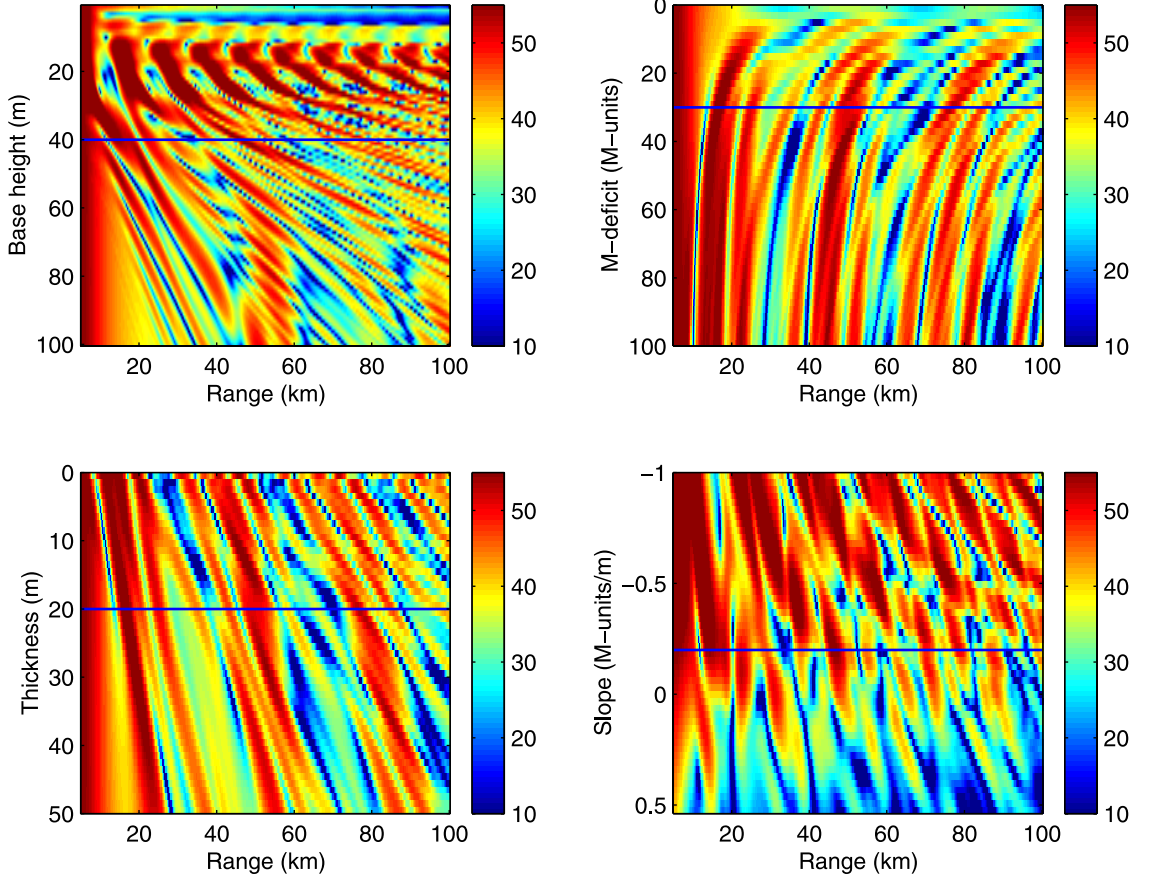


**Figure 8.** Sensitivity to varying environmental parameters of the clutter return. The plots show the clutter power returns (dB, equation (7)). The horizontal line indicates the baseline value held fixed while the other parameters are varied.

(6) provides an improvement in the inversion results, we used  $c_{\text{lap}} = 0.118$  M units/m. The actual value of the left side in equation (6) and the used slope  $c_{\text{lap}}$  could likely be derived from climatology.

### 3.3. Propagation and Radar Model $H_{\text{prop}}$

[44] In the Appendix, it is shown that in the absence of receiver noise, the received signal power from the clutter can be modeled as

$$p_{\text{obs}}(r) = -2L(r, \mathbf{M}^{\text{true}}) + 10 \log_{10}(r) + \sigma^{\circ}(r) + C, \quad (7)$$

where  $\mathbf{M}^{\text{true}}$  is the unknown, true, range-and-height-dependent refractive environment,  $L$  is the propagation loss (dB),  $\sigma^{\circ}(r)$  is the true, unknown, range-dependent radar cross section of the sea surface at range  $r$ , and  $C$  takes into account radar parameters, etc.

[45] In our model, we assume neither  $C$  nor  $\sigma^{\circ}$  are known a priori. Thus we define the un-normalized power modeled clutter power as  $p'(r, \mathbf{m})$  where

$$p'(r, \mathbf{m}) = -2L(\mathbf{m}_r) + 10 \log_{10}(r), \quad (8)$$

while the vector of the values of  $p'(r, \mathbf{m})$  corresponding to the discrete ranges of interest is  $\mathbf{P}'_c(\mathbf{m})$ .

[46] The model parameter vector  $\mathbf{m}$  maps uniquely into  $\mathbf{M}$  via  $\mathbf{H}_{\text{env}}(\mathbf{m})$ , so the modeled clutter power value of  $\mathbf{P}$  can be referred to as either  $\mathbf{P}(\mathbf{m})$  or  $\mathbf{P}(\mathbf{M})$ . However, the true environment  $\mathbf{M}^{\text{true}}$  and that measured by the helicopter  $\mathbf{M}^{\text{helio}}$  have components that are not modeled in  $\mathbf{H}_{\text{env}}$  and can only be represented as  $\mathbf{P}(\mathbf{M}^{\text{true}})$  or  $\mathbf{P}(\mathbf{M}^{\text{helio}})$ , respectively.

### 3.4. Objective Function

[47] It is assumed that the difference (dB) between the observed  $\mathbf{P}'_c^{\text{obs}}$  and modeled  $\mathbf{P}'_c(\mathbf{m})$  clutter is Gaus-

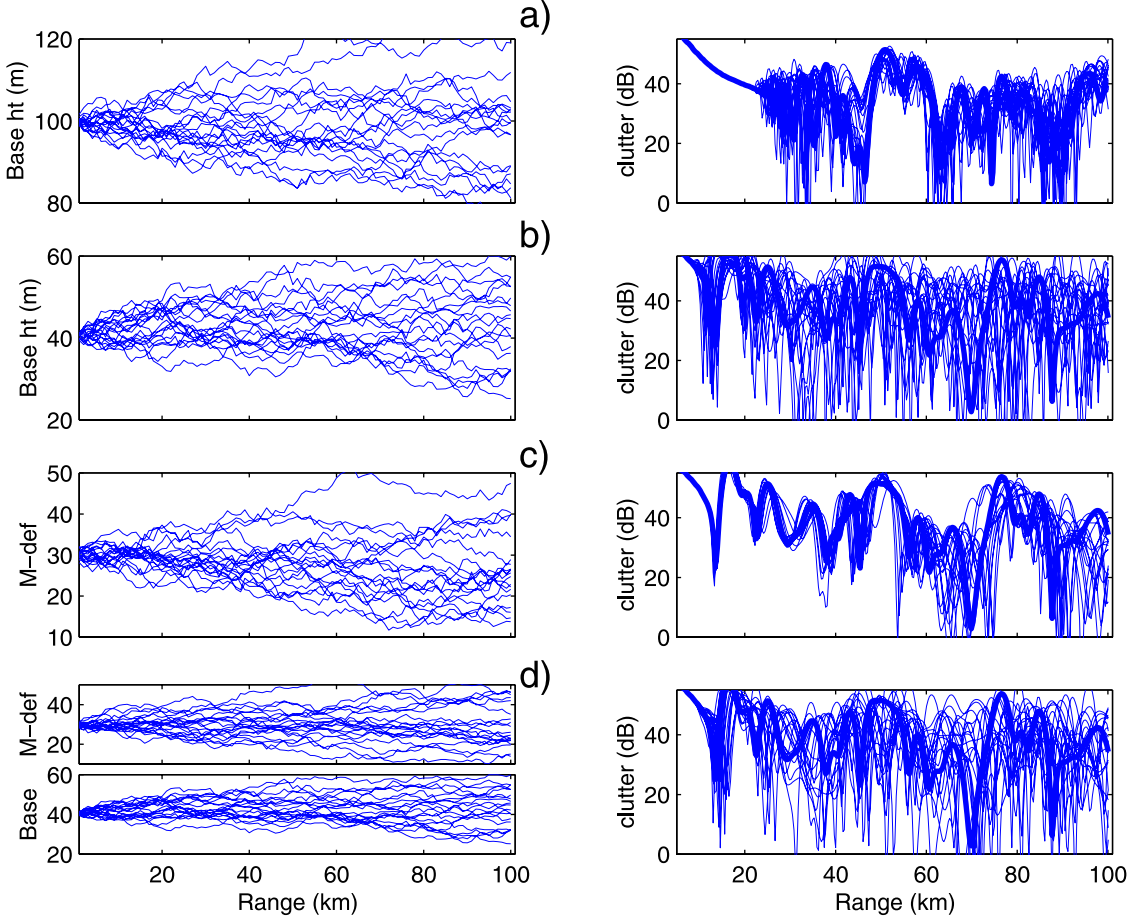


**Figure 9.** Simulation of clutter returns (right column) based on a Markov chain random variation in both base height and M deficit for 20 realizations (left column). (a) Variation in base height from 100 m; (b) variation in base height from 40 m; (c) variation in M deficit from 30 M units; and (d) variation in both base height from 40 m and M deficit from 30 M units. The thick line in the clutter profile is based on the range independent baseline profile.

sian. This leads to a simple least squares objective function:

$$\phi(\mathbf{m}) = \mathbf{e}^T \mathbf{e}, \quad (9)$$

where

$$\mathbf{e} = \mathbf{P}_c^{\text{obs}} - \mathbf{P}_c(\mathbf{m}) - \hat{T} \quad (10)$$

$$\hat{T} = \bar{\mathbf{P}}_c^{\text{obs}} - \bar{\mathbf{P}}_c(\mathbf{m}), \quad (11)$$

and the bar denotes the mean across the elements in the vector (i.e., the mean over the ranges considered).  $\hat{T}$  is an estimated normalization constant that for each realization of  $\mathbf{m}$  is adjusted so that the objective function only depends on the variation in clutter return but not on the

absolute level of the clutter return. In effect,  $\hat{T}$  is an estimate of  $[\sigma^0 + C]$  that is associated with each replica field. The objective function equation (9) is sensitive to the range-dependent variation in the clutter level, but not its absolute level.

### 3.5. Radar Cross Section

[48] Assumptions about the radar cross section are essential for the RFC inversions, especially the range and grazing angle dependency. Despite the considerable progress in low grazing angle backscatter modeling (see, e.g. the special issue on low-grazing angle backscatter [Brown, 1998; Toporkov *et al.*, 1999; Voronovich and Zavorotny, 2000; West, 2000; Torrungrueng *et al.*, 2000]) this ability is only used indirectly as it will complicate the inversion considerably. The output of linked weather,

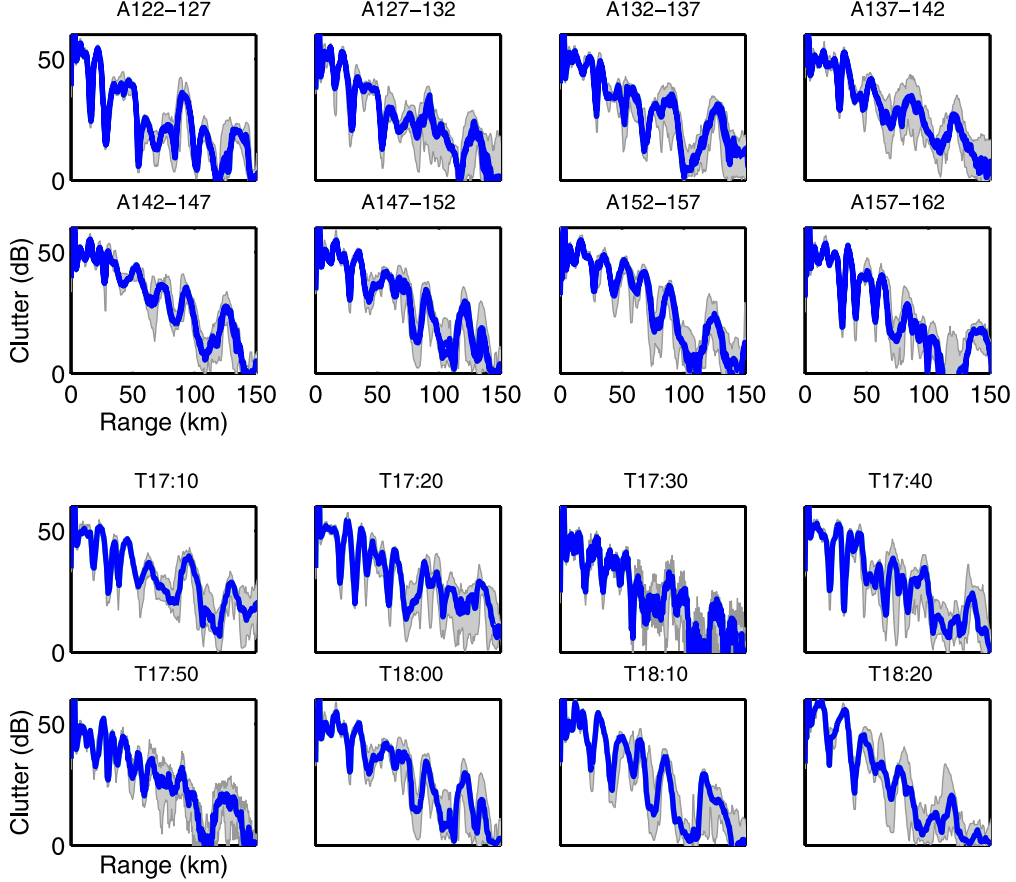


**Figure 10.** Clutter returns as a function of range for different angles (top) and times (bottom). The shaded area is the envelope of 13 returns in a  $5^\circ$  interval (i.e.,  $0.4^\circ$  increment), and the dark line is the median. In the top figure, the  $5^\circ$  angle intervals are for azimuths centered at  $125^\circ$ – $160^\circ$  at time 13:00 EST. In the bottom figure, the time interval is 11:10–12:20 EST.

wave, clutter and propagation models may eventually be brought into the refractivity inversion algorithms. However, assessing the goodness of the linked models should precede that step and such investigations are only beginning [see Wagner *et al.*, 2001].

### 3.5.1. Range Dependence

[49] Equation (7) shows that RFC is sensitive to  $\sigma^0(r)$ . If too much freedom is allowed for  $\sigma^0(r)$  then this will hamper our ability to estimate the refractivity profile. Because of nonlinearities it is possible to invert for some variations in  $\sigma^0(r)$ . We are at present neglecting all range variations in  $\sigma^0(r)$ .

[50] For the SPANDAR data the scale of variability of the sea clutter radar cross section, over the ranges of 10 to 60 km are on the order of several dB (section 5.4). But the propagation loss contour diagrams shows the 2-way propagation loss over ranges as small as 10 km being on the order of 30 dB or more (sections 5.1–5.3). Thus for the cases considered here, the first-order problem is

developing a modeling of the refractive environment that can match the observed clutter intensifications. The horizontal variations in the sea-clutter radar cross section are a second-order problem.

[51] The relative contribution of sea clutter RCS vis a vis that of the propagation is problem dependent. Exercising a sea clutter RCS model such as GIT will yield that the sensitivity of the sea clutter RCS to the wind speed is greater at low wind speeds (0–3 m/s) than at the wind speeds associated with the cases considered here (4–7 m/s). Thus in an environment such as the Persian Gulf where surface based ducts are common but the wind speeds are typically lower, the horizontal variability of the sea clutter RCS may become more important.

### 3.5.2. Grazing Angle

[52] For vertical polarization there is still some question as to whether the grazing angle dependence is  $\psi^0$ ,  $\psi^4$  or some value in between [see Barrick, 1998; Tatarski and Charnotskii, 1998]. For inferring evaporation duct

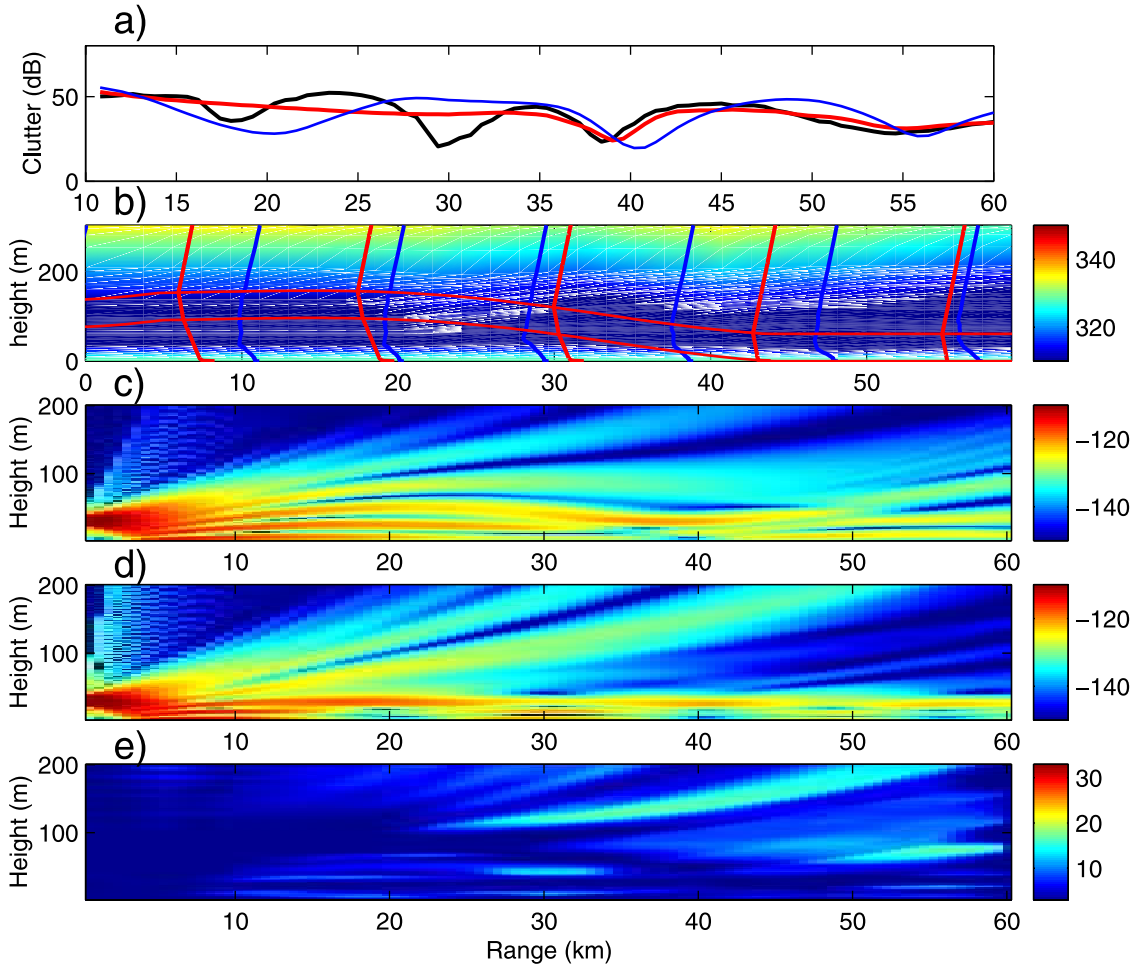


**Figure 11.** Inversion based on the clutter return shown in Figure 2 along azimuth  $150^\circ$ . (a) The clutter return (dB) as observed by the radar data (black), the modeled return using the inverted profile (red), and modeled return from the observed profile (blue); (b) observed profiles measured from helicopter (blue and color-contour) and inverted profiles (red); (c) coverage diagram (dB) corresponding the inverted profiles; (d) coverage diagram (dB) based on helicopter profiles. (e) difference (dB) between coverage diagrams Figures 11c and 11d.

heights from radar sea echo, Rogers *et al.* [2000] found that while their data did not provide a definitive answer to the grazing angle dependency, the use of  $\sigma \propto \psi^0$  in the duct height estimation algorithm generated better results. This model is chosen here.

### 3.5.3. Radar Cross-Section Statistics

[53] If the refractivity profiles measured via the helicopter are assumed accurate representations of the true environment, it is possible to assess how well the inversion algorithm is estimating  $[\sigma^\circ(r) + C]$  without having measured those quantities directly. We can manipulate equations (7), (8), and (11) to obtain,

$$[\sigma^\circ(r) + C] - T = p_{obs}(r) - 10 \log(r) - \hat{T} + 2L(r, \mathbf{M}^{\text{true}}). \quad (12)$$

$T$  is the true value of the bias. Furthermore, by equation (11), the term  $p(r, \mathbf{M}^{\text{true}}) - p(r, \hat{\mathbf{M}})$  drops out when we average over the ranges used in the computation of  $T$  to give:

$$[\bar{\sigma}^\circ + C] - T = \frac{2\bar{L}(r, \mathbf{M}^{\text{true}})}{2\bar{L}(r, \mathbf{M}^{\text{helio}})} - \frac{2\bar{L}(r, \hat{\mathbf{M}})}{2\bar{L}(r, \hat{\mathbf{M}})}. \quad (13)$$

The mean and standard deviation of the right-hand sides of equations (12) and (13) represent the bias and standard error of  $T$  in estimating  $[\sigma^\circ(r) + C]$  and  $[\bar{\sigma}^\circ + C]$ , respectively.

### 3.6. Optimization

[54] The Simulated Annealing/Genetic Algorithm code [Gerstoft, 1997; Gerstoft *et al.*, 2000] is used to optimize

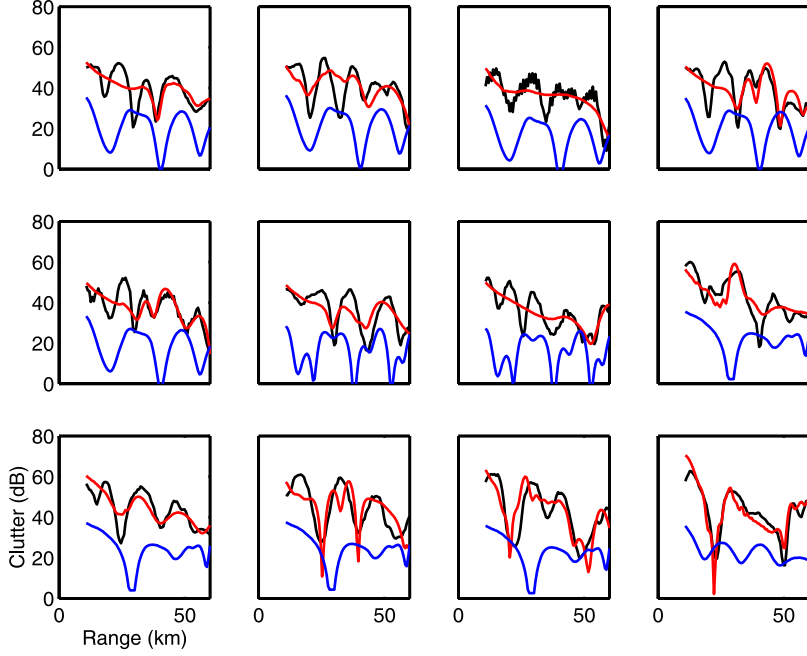


**Figure 12.** The clutter returns as observed by the radar data (black), the modeled returns using the inverted profile (red), and the modeled clutter returns for the helicopter profiles (blue, offset 20 dB) are shown for clutter maps 7–18 (corresponding to 10-min time intervals from 12:10–13:50 EST). The curves are normalized so that they have the same mean. The average absolute error in predicting the clutter is 4.7 dB for the inversions and 8.9 dB for the helicopter profiles.

equation (9). The GA-search parameters were: parameter quantization 128 values; population size 64; reproduction size 0.5; cross-over probability 0.05; number of iterations for each population 2000; and number of populations 10. Thus 20000 forward modeling runs were performed for each inversion. For further information about the use of GA for parameter estimation, see Gerstoft [1994].

## 4. Sensitivity

### 4.1. Sensitivity to Range-Independent Parameters

[55] Figure 8 shows the modeled clutter returns, equation (7), as a function of range ( $x$ -axis) and variation of individual parameters ( $y$ -axis). Clearly, changes in the inversion base height  $z_b$ , thickness  $\Delta z$ , and mixed layer slope  $dM/dz$ , shift the location of intensifications. Additionally, the size of the horizontal shift in the location of an intensification increases nearly linearly as a function of the intensification's original range. One might hypothesize that in performing the inversions, one really is inverting a super-parameter that is a linear combination of  $z_b$ ,  $\Delta z$ , and  $dM/dz$ . As long as a surface duct is created, the M deficit ( $\Delta M$ ) is not an important parameter. In the present simulation, this happens for a  $\Delta M$

value of about 20–30 M units. With a negative slope in the mixed layer, a surface channel will always be created causing high clutter return. But for positive slopes, the creation of surface duct depends on the  $z_b$ ,  $\Delta z$ , and  $\Delta M$ .

### 4.2. Sensitivity to Range Dependency

[56] From the modified refractivity profiles in Figure 3, it is clear that these show a range (and temporal) dependence. This effect is simulated by modeling variations in range as a Markov process as shown in Figure 9. For each kilometer, the profile was updated using a Gaussian distribution with a standard deviation of 1 (m or M units).

[57] In the top pair of plots in Figure 9, the random variations in  $z_b$  about the starting value of 100 m provide some corruption to the major intensification between 45 and 60 km, but the intensification is still recognizable. On the other hand, in the second pair of plots where the variations is starting from  $z_b = 40$  m, features occurring beyond about 30 km are difficult to associate with features in the horizontally homogeneous case. This illustrates the state dependence of the response to parameter variations. Clearly, the random variations in  $\Delta M$  do not introduce as much variability as those in the base height. The lowest plots correspond to joint, independent

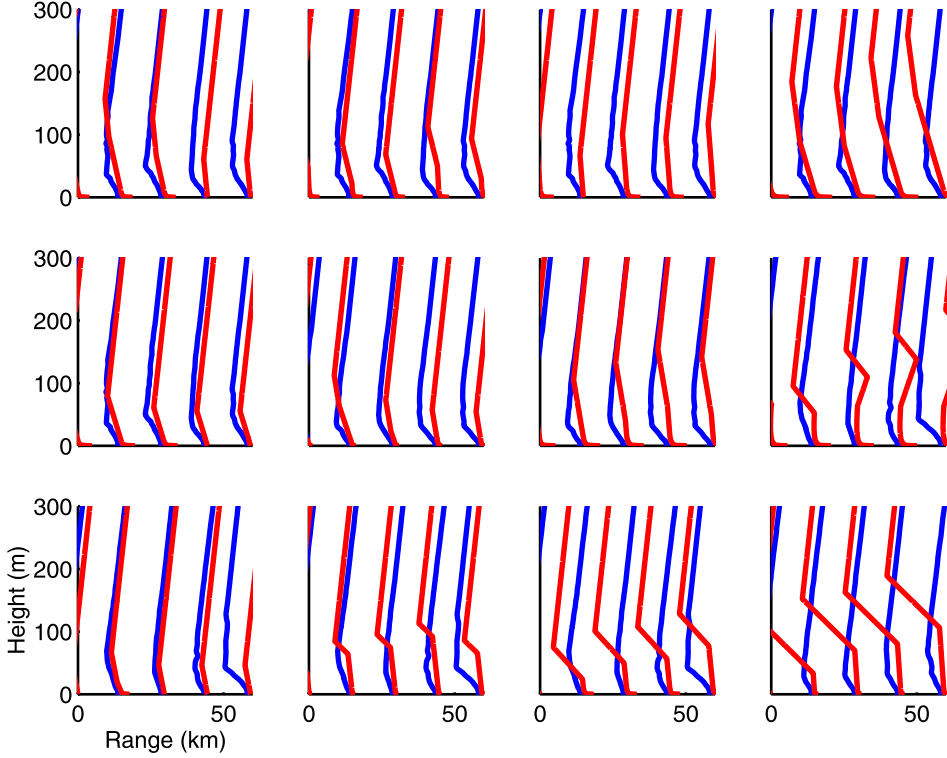


**Figure 13.** Observed (blue) and estimated (red) refractivity profiles for clutter maps 7–18.

variations in the  $\Delta M$  and base height. The variability is dominated by that induced from the base height.

#### 4.3. Observed Azimuthal and Temporal Variability of Clutter Returns

[58] The envelopes and median values of Clutter-return data from the SPANDAR are plotted in Figure 10. The SPANDAR radar has an azimuthal resolution of  $0.4^\circ$ . By analyzing the returns over larger azimuthal resolution,  $5^\circ$ , corresponding to 13 returns, an understanding of the variation in clutter is obtained. The upper series of plots corresponds to envelopes over different  $5^\circ$  sectors from the same clutter map. Plots in the lower series correspond to envelopes over a single  $5^\circ$  sector that were obtained at 10-minute intervals. The broadening of the envelopes with respect to range is possibly explained either by variations in the mean value (with respect to range) of the parameters (Figure 8 illustrates a case), or by variations in range as illustrated in Figure 9.

## 5. Inversion of SPANDAR Data

[59] The SPANDAR data, section 2, is used to demonstrate the feasibility of estimating the range-dependent refractive structure. In section 5.1, a single clutter map is inverted, and in section 5.2, a sequence of 12 frames is

analyzed. This leads to a constraint on the  $M$  profile as described in section 5.3.

[60] The observed clutter data  $\mathbf{P}_c^{\text{obs}}$  is taken from the  $150^\circ$  radial and 10–60 km range using clutter maps similar to Figure 2. Twelve maps (clutter maps 7–18) at 10-min intervals from 12:10–13:50 EST were used.

#### 5.1. Analysis of a Single Frame

[61] Figure 11 summarizes the inversion and assessment of the inversion results for a single frame. First, the clutter  $\mathbf{P}_c^{\text{obs}}$  along azimuth  $150^\circ$  and 10–60 km in range is extracted from the clutter map (Figure 2) and shown as a solid line in Figure 11a. Clutter-return intensifications are seen at around 25, 35, and 45 km. Optimizing the fit between the replica  $\mathbf{P}_c(\mathbf{m})$  and the observed data with respect to the environmental parameters in Table 2 was carried out. The best matching replica is shown as red, and for reference, the modeled clutter returns from the helicopter profiles are shown in blue. The objective function, equation (9), is only concerned with minimizing the error and only indirectly is there optimization for the location and number of peaks. The inversion can visually be judged by examining how the peaks in the replica are matched. Based on the location of maxima and minima in Figure 11a, the inversion only matches well at longer ranges.

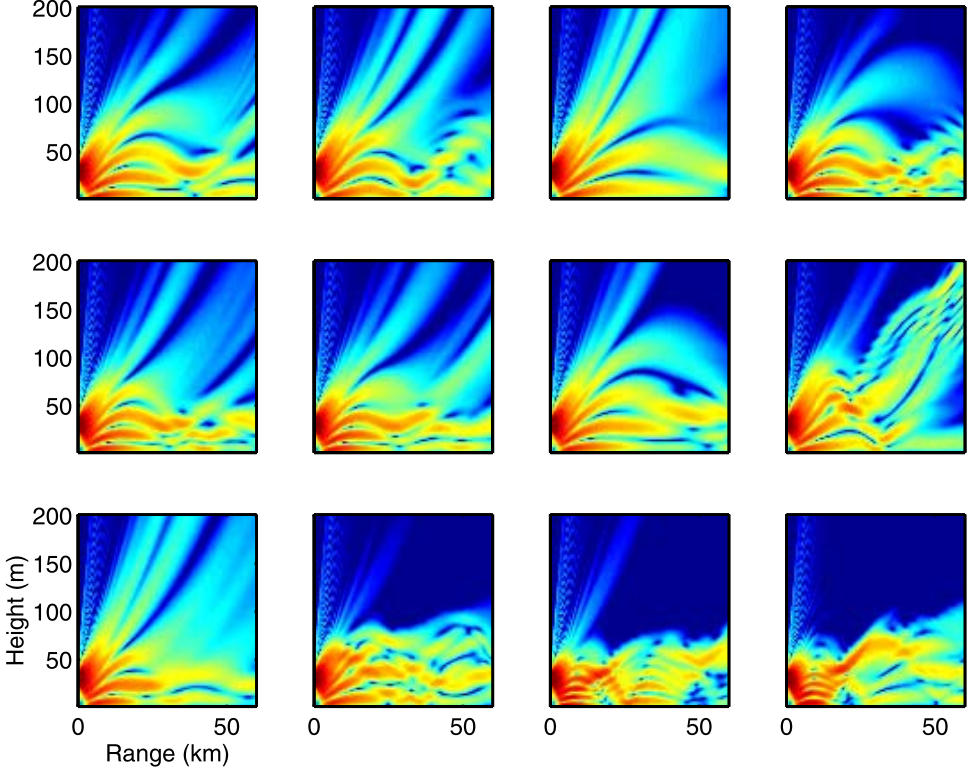


**Figure 14.** The coverage diagram (dB) based on the inverted profiles for clutter maps 7–18.

[62] The second plot (Figure 11b) shows the estimated refractivity profiles (red) along with the helicopter refractivity profiles (blue, color-contour). Because this is an under determined problem, the best fit might not correspond to the true profile. An equivalent profile that gives the best match to the clutter return is obtained. The next two plots show the modeled propagation loss for the optimal environment and the helicopter profiles, respectively. The difference of these two (bottom plot) gives an indication of how well the inverted profile is able to predict the propagation loss. This plot has been medium filtered based on a  $10\text{ m} \times 6\text{ m}$  box in range and height. Comparing this plot with the variation shown in Figure 5 indicates that the inversion is of reasonable quality.

## 5.2. Inversion Without Constraints

[63] The clutter returns extracted from the clutter maps are shown in Figure 12 (black). Notice that the clutter returns vary significantly over a 10-min interval. For reference, the clutter returns (blue) also are calculated from the helicopter profiles closest in time. Four profiles of Figure 3 were used: helicopter profile 5 for clutter maps 7–11, helicopter profile 6 for clutter-maps 12–13,

helicopter-profile 7 for clutter maps 14–17, and helicopter-profile 8 for clutter-map 18. It is clear that the clutter return modeled from the measured refractivity profiles do not show a perfect match, but the main features are captured. It is expected that the nulls mainly are due to destructive interference in the wave propagation. Not all environmental information relevant for the propagation is captured in the helicopter-profiles, so these should not be treated as “ground truth.”

[64] Based on the inversions, the range-dependent profiles in Figure 13 were obtained. It can be seen that the estimated profiles (red) have a tendency to overestimate the M excess, defined as  $M(0) - M(z_{\text{top}})$ , where  $z_{\text{top}}$  is the top of the trapping layer. This is because once a wave is trapped in the duct, the value of the M excess is not important, as illustrated in Figures 8b and 8d.

[65] To assess the quality of the inversions, the corresponding clutter returns (red lines in Figure 12) and coverage diagrams (Figure 14) were generated.

[66] The ratio between the fields based on the clutter inversions (Figure 14) and the fields from the helicopter runs (frames 5–7 of Figure 4) is shown in Figure 15. While the difference in the first 50-m in height is quite small, the difference for the propagation above the duct

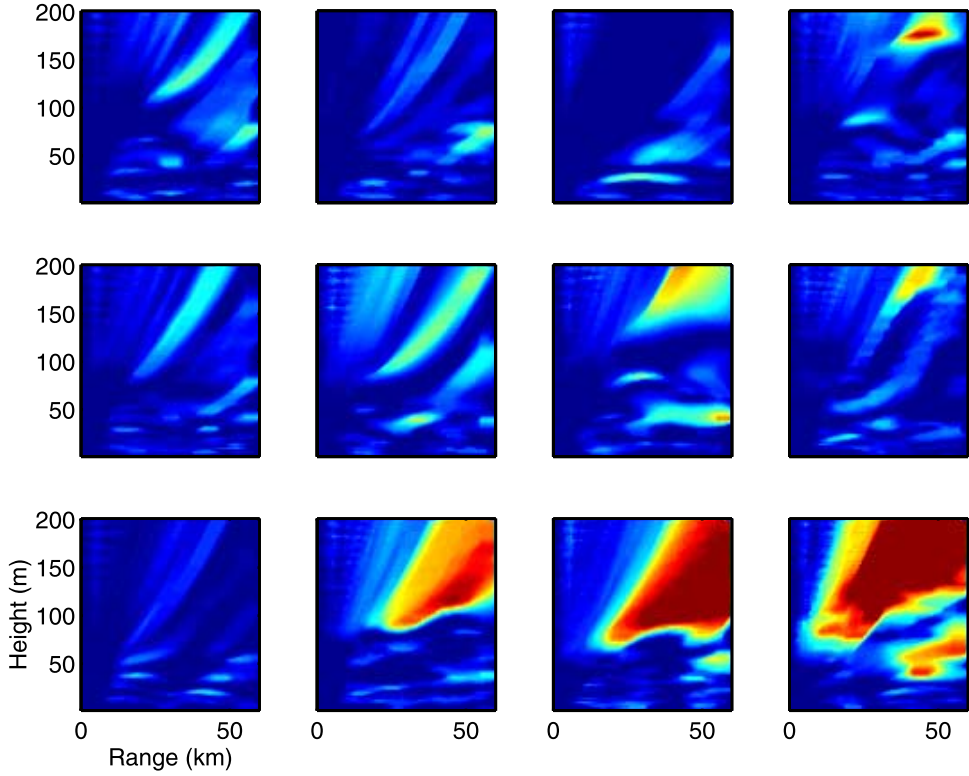


**Figure 15.** The difference (dB) between the fields from the inversion (Figure 14) and the helicopter-based field (Figure 4).

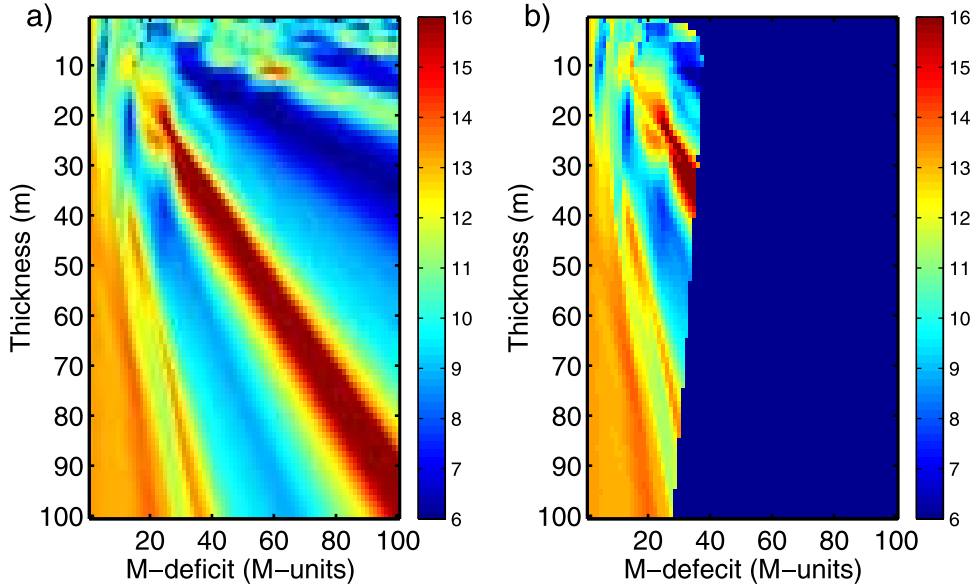


**Figure 16.** Ambiguity surface (dB) of thickness versus M deficit based on data from clutter map 18. The baseline environment is the solution of the unconstrained optimization. (a) With no constraint; (b) with constraint (equation (6)). The dark blue area in Figure 16b indicates invalid solutions. Red indicates a better fit.

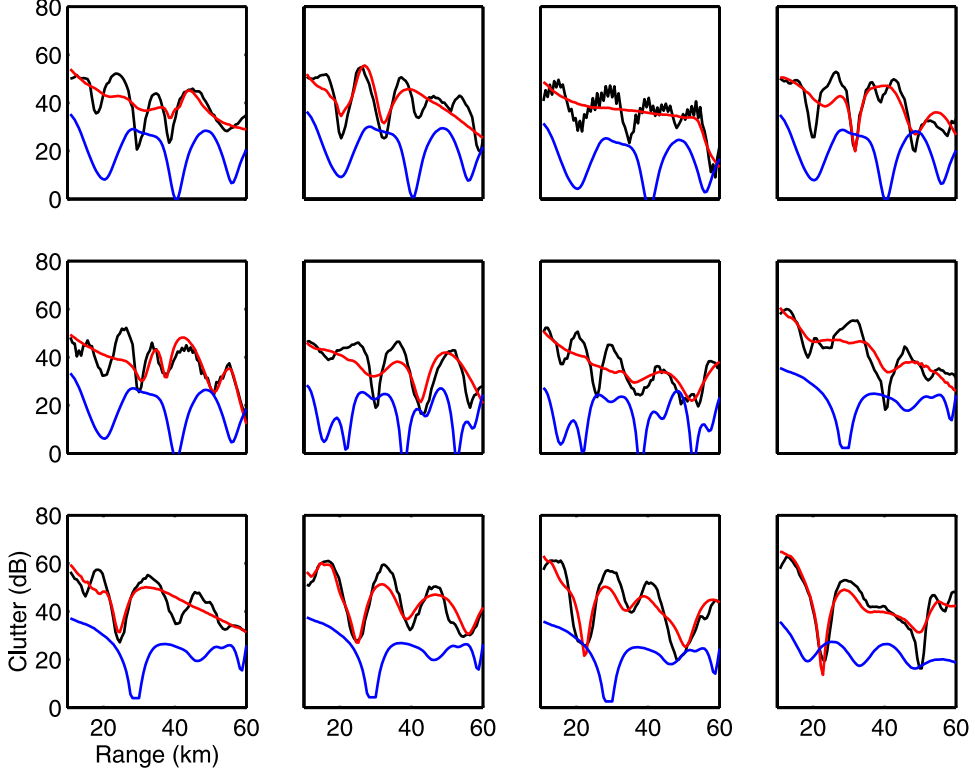


**Figure 17.** The clutter returns as observed by the radar data (black), the modeled returns using the inverted profile (red), and the modeled clutter returns for the helicopter profiles (blue, offset 20 dB) are shown for clutter map 7–18. The curves are normalized so that they have the same mean.

is large. This is because the value of the M excess is important for how much energy radiates out of the duct but is not well-determined by the inversion.

### 5.3. Inversion With Constraints

[67] A contour plot (Figure 16a) of the value (dB) of the objective function equation (9) between thickness and M deficit for data from clutter map 18, where a large M deficit was estimated in the inversion, reveals that the two parameters are strongly correlated for M deficits larger than about 60 M units, and that we are insensitive to the combination of thickness and M deficit. As shown in Figure 16b, implementing the constraint described in section 3.2.1 reduces the search space so that only the smaller M deficit is allowed. This constraint will influence all inversion parameters, especially the M deficit and the mixed-layer slope.

[68] The result of the constrained inversion is shown in Figures 17, 18, and 19. It is seen that the fit to the clutter returns is not changed significantly (Figure 17). However, the retrieved profiles appear more reasonable (Figure 18). Furthermore, the difference between the propagation loss

from the helicopter profiles and inverted profiles is quite low even above the duct (Figure 19).

### 5.4. Statistics of Errors and Evaluation

[69] We define the bias  $b$  in the prediction of one-way propagation loss  $L$  (dB) in the range-height domain  $D$  as

$$b = \frac{2}{N} \sum_{r,z \in D} \left[ -L(\hat{\mathbf{M}}, r, d) + L(\mathbf{M}^{\text{helo}}, r, d) \right] \quad (14)$$

where  $N$  is the number of points in  $D$ . In Table 3, biases are calculated for two domains corresponding to the duct and a large domain consisting of the duct plus the area above the duct (0–50 m  $\times$  0–100 km and 0–200 m  $\times$  0–100 km, respectively), for both the unconstrained and constrained models. It is clear that for frame 16–18, there is substantial error in using the unconstrained  $\hat{\mathbf{M}}$  for the larger domain. When the duct unconstrained cases are considered, no individual bias has a magnitude greater than 8 dB, and the mean bias is –2.8 dB. This suggests that most of the error is in the region above the duct, as also indicated by Figure 15. The amount of energy that leaks out of the duct

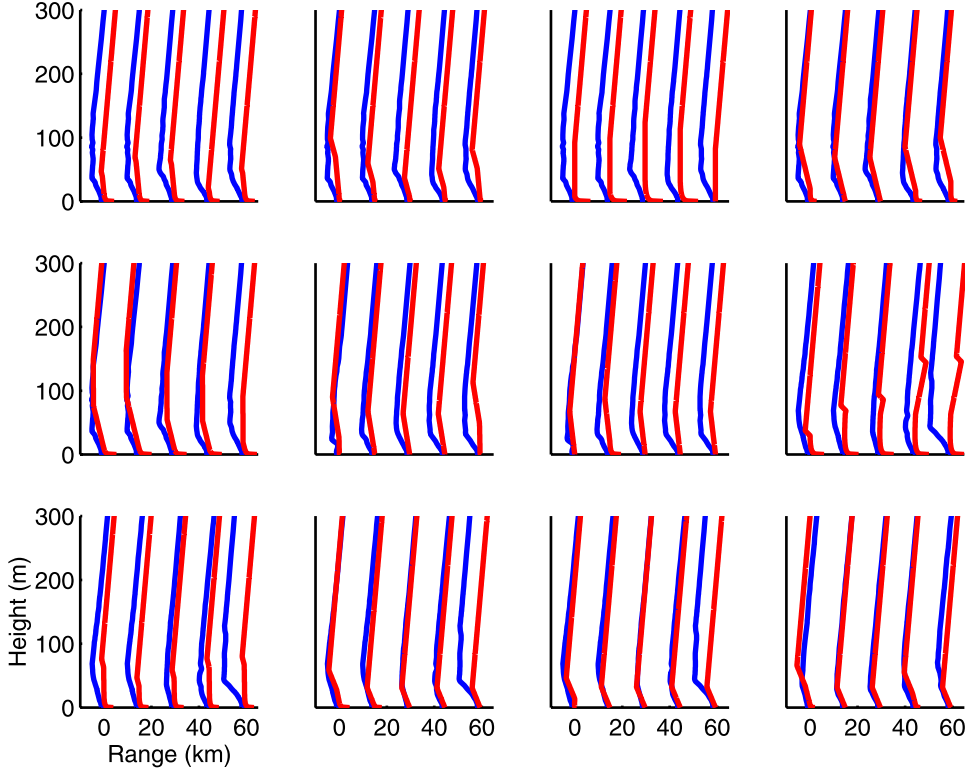


**Figure 18.** Observed (blue) and estimated (red) refractivity profiles for clutter map 7–18.

depends on the value of the M deficit, but the total energy in the duct is nearly constant as long as the M deficit is so large that the energy is trapped. When the constrained model is used, the mean and standard deviation of the biases across the data are small (both less than 4 dB).

[70] The helicopter profiles are not easy to obtain in practice. In fact, having a single Radiosonde or rocketsonde at the midpoint of the transmission path of interest might be considered a best case scenario. A single sounding is simulated by assuming the vertical refractivity profile at all ranges equal to the midrange helicopter refractivity profile. Our benchmark is the accuracy of these “range-independent” environments in estimating the propagation loss that is predicted using the range-dependent soundings. The benchmark was not very sensitive to which profile was used for the range-independent environment.

[71] Error statistics for 2-way propagation loss (dB) for the RFC algorithm and the benchmark, considering the duct domains ( $0\text{--}50\text{ m} \times 0\text{--}100\text{ km}$ ) and a large domain ( $0\text{--}200\text{ m} \times 0\text{--}100\text{ km}$ ), are given in Table 4. The time delay is obtained by using an older Radiosonde. It is seen that the errors increase with time

delay; the constrained and unconstrained gives about the same error; and the larger domain gives a slightly larger error. For the cases considered, Propagation-loss values based on radar-inferred refractivity structures approach what might be obtained using a single representative sounding.

[72] We now consider how good the a priori knowledge of  $\sigma^o$  would have to be in order to be an aid for the inversion. Figure 20 is a plot of the mean and envelope defined by the standard deviation of equation (12) over the constrained cases. The trend that the standard deviation decreases with range is realistic; it implies that  $\sigma^o$  may be decreasing about 5 dB over the 50-km range. The range-averaged value of the mean (corresponding to equation (13)) is  $-2.8\text{ dB}$ , representing the amount  $\hat{T}$  is underestimating  $[\bar{\sigma}^o + C]$ . This is consistent with over estimating duct strength. The value of  $T$  depends on parameter vector  $\mathbf{m}$ , equation (11), and varies over several decades (dB). Clearly, the  $\hat{T}(\mathbf{m})$  are tightly distributed about the true values of  $[\bar{\sigma}^o + C]$ . Given the small uncertainty in  $[\bar{\sigma}^o + C]$ , it might be difficult to use a priori estimates of  $[\bar{\sigma}^o + C]$  (the former term presumably calculated from wind fields generated by a numerical weather prediction model)

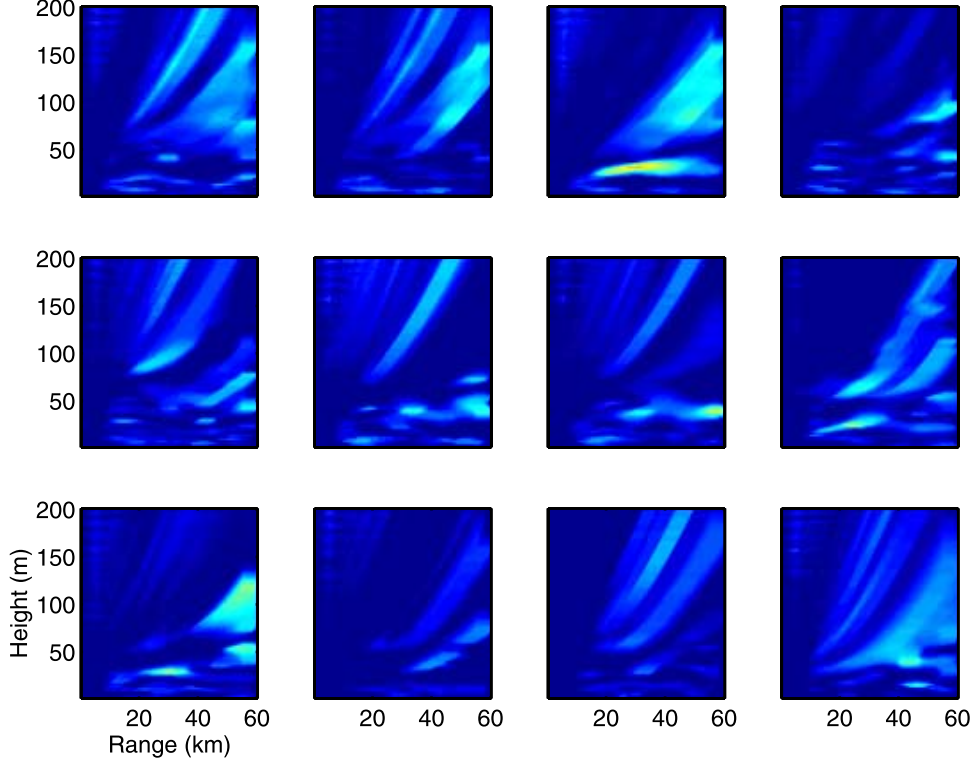


**Figure 19.** The difference (dB) between the fields from the inversion and the helicopter-based fields (Figure 4).

with sufficient accuracy to improve the inversion results.

## 6. Summary

[73] An implementation for the inference of refractivity parameters from radar clutter has been described. A multi-parameter range-dependent parameterization was introduced and the use of a genetic algorithm via the SAGA inversion code was employed to handle the large search space. We find that within the duct itself, the accuracy of the radar-inferred propagation-loss values approaches that of loss values calculated using a midpath sounding. This finding is based on an analysis that would tend to favor the midpath sounding. But, the ability of the radar-inferred loss values to estimate the loss values in the shadow zone above the duct is more limited. It is demonstrated that inclusion of prior information alleviates this problem to a large degree.

[74] The parameterization and search bounds that were used could easily accommodate refractivity profiles found in other regions of the world. Furthermore, as the sensitivity examination in section 4 showed, the relatively low ducts in these data tend to stress the inversion algorithm more than the alternative of higher

ducts. Thus we have no reason to suspect that the performance of the algorithm will degrade when implemented using data where the typical refractivity structures differ from the cases examined here.

**Table 3.** Two-Way Propagation Loss Bias<sup>a</sup>

Clutter Map	0–200 m, U	0–200 m, C	0–50 m, U	0–50 m, C
7	1.2	-2.6	-2.3	-0.8
8	-0.6	-1.4	-0.7	-0.9
9	-3.2	-3.3	-0.9	5.0
10	5.0	3.8	-3.3	-3.0
11	1.8	2.6	-2.8	-3.1
12	6.0	4.2	-7.7	-8.1
13	6.8	1.9	-7.8	-6.7
14	4.0	1.0	2.7	3.3
15	-0.0	1.6	-1.0	-0.2
16	17.3	2.6	-1.9	1.1
17	25.5	0.6	-1.6	1.8
18	29.2	-1.0	-5.8	0.1
$\mu$	7.7	0.8	-2.8	-1.0
$\sigma$	10.5	2.4	3.0	3.8

<sup>a</sup>Averaged difference in 2-way propagation loss calculations based on radar-inferred refractivity and calculated from the helicopter soundings. The duct domain (0–50 m  $\times$  0–100 km) and a larger domain (0–200 m  $\times$  0–100 km) are considered as unconstrained (U) and constrained (C) solutions.

**Table 4.** Average Over All Clutter Inversion of Absolute Difference Between Loss Determined by Helicopter Soundings and Either the RFC or a Single Sounding at Midpath<sup>a</sup>

Time Delay, hour	RFC, dB	RFC Constraint, dB	Midpath, dB
Coverage: 0–200 m × 0–100 km			
0	9.4	6.0	5.0
2	-	-	5.7
4	-	-	6.4
Coverage: 0–50 m × 0–100 km			
0	5.1	5.2	3.8

<sup>a</sup>The difference is for the duct domain (0–50 m × 0–100 km) and a larger domain (0–200 m × 0–100 km).

[75] The wind speeds for the cases examined are about 5 m/s. The Georgia Institute of Technology (GIT) clutter model [Paulus, 1990], essentially a compilation of empirical data, shows that at lower wind speeds there is a greater horizontal variability of  $\sigma^{\circ}$ . Additionally, lower winds speeds will lead to smaller values of  $\sigma^{\circ}$ , thus resulting in a greater portion of the clutter returns being below the noise floor of the receiver. Both of these factors will negatively impact the inversion results. Thus the observed performance of the algorithm might not generalize to lower wind speeds.

## Appendix A: Manipulating the Radar Equation

[76] From *Barton* [1988] or *Sauvageot* [1992] the received power  $S$  from a target of cross section  $\sigma$  at range  $r$  with free space propagation is

$$S = \frac{P_t G_t G_r \lambda^2 f^4(\Delta_\theta, \Delta_\phi), F^2 \sigma}{(4\pi)^3 r^4}. \quad (\text{A1})$$

where  $P_t$  is the transmitted power,  $G_t$  and  $G_r$  are the respective transmit and receiving antenna gains, and  $\lambda$  is the wavelength. The term  $f(\Delta_\theta, \Delta_\phi)$  is the antenna pattern propagation factor where  $\Delta_\theta$  and  $\Delta_\phi$  are the deviations from beam center ( $f(0, 0) = 1$  by definition). The term  $F$  is the propagation factor which accounts for deviations from free space propagation not accounted for by the antenna pattern. Note that Barton's  $F$  is effectively  $f^2 F$  in the sense that we use it and Sauvageot uses the symbol  $L$  where we use  $F$ .

[77] The inputs to modern propagation models include the antenna pattern propagation factor, elevation angle, frequency and arguments for environmental factors including refractivity, gaseous absorption, surface reflection coefficients, terrain profile, etc. The loss value they output accounts for  $f$ ,  $F$ , and  $L_{fs}$  such that

$$L = \frac{L_{fs}}{f^2 F}. \quad (\text{A2})$$

Using (A2) and the formula for free-space propagation

$$L_{fs} = \frac{(4\pi)^2 r^2}{\lambda^2},$$

one arrives at:

$$S = \frac{P_t G_t G_r 4\pi \sigma}{L^2 \lambda^2}. \quad (\text{A3})$$

[78] To calculate the received power from sea clutter  $P_c$ , we use the relationship  $\sigma = A_c \sigma^{\circ}$ , where  $A_c$  is the

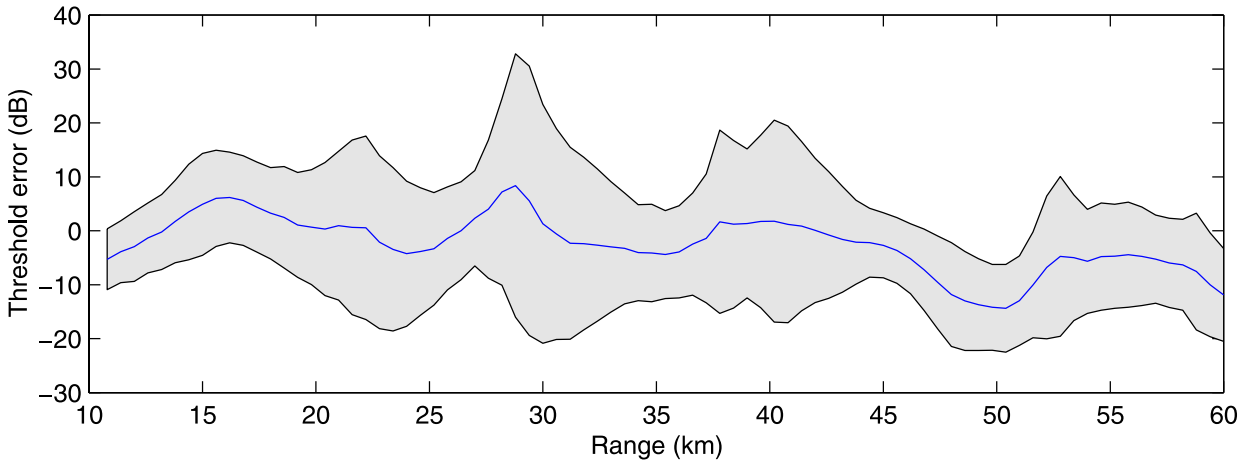


**Figure 20.** Mean (blue) of threshold error (dB) as defined by equation (12) for the constrained cases. Plus/minus a standard deviation is indicated by the gray area.

illuminated area and  $\sigma^o$  is the sea clutter's normalized radar cross section, to rewrite equation (A3) as

$$P_c = \frac{P_t G_t G_r 4\pi A_c \sigma^o}{L^2 \lambda^2}. \quad (\text{A4})$$

At low grazing angles,  $A_c$  is a linear function of  $r$ , thus we can rewrite equation (A4) in the form

$$P_c = \frac{C \sigma^o r}{L^2}. \quad (\text{A5})$$

where  $C$  accounts for all of the constant terms in (A4). Letting the symbols  $P_c$ ,  $C$ ,  $\sigma^o$ , and  $L$  represent the associated values in dB as opposed to real numbers, we can rewrite equation (A5) as

$$P_c = -2L + \sigma^o + 10\log_{10}(r) + C. \quad (\text{A6})$$

[79] **Acknowledgments.** This research was supported by the Office of Naval Research, Codes 321 and 322.

## References

- Anderson, R., S. Vasudevan, J. Krolik, and L. T. Rogers, Maximum a posteriori refractivity estimation from radar clutter using a Markov model for microwave propagation, paper presented at the International Geoscience and Remote Sensing Symposium, Sydney, Australia, Int. of Electr. and Electron. Eng., New York, July 2001.
- Barrick, D. E., Grazing angle behavior of scatter and propagation above any rough surface, *IEEE Trans. Antennas Propag.*, 46(1), 73–83, 1998.
- Barrios, A. E., A terrain parabolic equation model for propagation in the troposphere, *IEEE Trans. Antennas Propag.*, 42, 90–98, 1994.
- Barton, D. K., *Modern Radar System Analysis*, Artech House, Norwood, Mass., 1988.
- Brown, G. S., Special issue on low-grazing-angle backscatter from rough surfaces, *IEEE Trans. Antennas Propag.*, 46(1), 1–2, 1998.
- Dockery, G. D., Development and use of electromagnetic parabolic equation propagation models for US Navy applications, *Johns Hopkins APL Tech. Dig.*, 19, 283–292, 1998.
- Gerstoft, P., Inversion of seismoacoustic data using genetic algorithms and a posteriori probability distributions, *J. Acoust. Soc. Am.*, 95, 770–782, 1994.
- Gerstoft, P., *SAGA Users Guide 2.0: An Inversion Software Package*, SM-333, SACLANT Undersea Res. Cent., La Spezia, Italy, 1997. (Available at <http://www-mpl.ucsd.edu/people/gerstoft/saga/saga.html>.)
- Gerstoft, P., and C. F. Mecklenbräuker, Ocean acoustic inversion with estimation of a posteriori probability distributions, *J. Acoust. Soc. Am.*, 104, 808–819, 1998.
- Gerstoft, P., D. F. Gingras, L. T. Rogers, and W. S. Hodgkiss, Estimation of radio refractivity structure using matched field array processing, *IEEE Trans. Antennas Propag.*, 48, 345–356, 2000.
- Goldhirsh, J., and D. Dockery, Propagation factor errors due to the assumption of lateral homogeneity, *Radio Sci.*, 33(2), 239–249, 1998.
- Gossard, E. E., and R. G. Strauch, *Radar Observations of Clear Air and Clouds*, Elsevier Sci., New York, 1983.
- Haack, T., and S. D. Burk, Summertime marine refractivity conditions along coastal California, *J. Appl. Meteorol.*, 40, 673–687, 2001.
- Krolik, J. L., and J. Tabrikian, Tropospheric refractivity estimation using radar clutter from the sea surface, in *Proceedings of the 1997 Battlespace Atmospheric Conference, SPAWAR Sys. Command Tech. Rep.* 2989, 635–642, Space and Nav. Warfare Sys. Command Cent., San Diego, Calif., March 1998.
- Levy, M. F., *Parabolic Equation Methods for Electromagnetic Wave Propagation*, Inst. of Electr. Eng., London, 2000.
- Patterson, W., *Ducting Climatology Summary*, SPAWAR Sys. Cent., San Diego, Calif., 1992.
- Paulus, R. A., Evaporation duct effects on sea clutter, *Radio Sci.*, 38(11), 1765–1771, 1990.
- Richter, J. H., Structure, variability, and sensing of the coastal environment, in *Proceedings of the AGARD SPP Symposium on Propagation Assessments in Coastal Environments, Bremerhaven, Germany*, pp. 1.1–7.14, NATO AGARD, Neuilly-sur-Seine, France, Feb. 1995.
- Rogers, L. T., Likelihood estimation of tropospheric duct parameters from horizontal propagation measurements, *Radio Sci.*, 32, 79–92, 1997.
- Rogers, L. T., C. P. Hattan, and J. K. Stapleton, Estimating evaporation duct heights from radar sea clutter, *Radio Sci.*, 35(4), 955–966, 2000.
- Rowland, J. R., G. C. Konstanzer, M. R. Neves, R. E. Miller, J. H. Meyer, and J. R. Rottier, SEAWASP: Refractivity characterization using shipboard sensors, in *Proceedings of the Battlespace Atmospheric Conference, Tech. Doc.* 2938, pp. 155–164, RDT&E Div., Nav. Command Control and Ocean Surv. Cent., San Diego, Calif., Dec. 1996.
- Sauvageot, H., *Radar Meteorology*, Artech House, Norwell, Mass., 1992.
- Stahl, R. W., and D. A. Crippen, *An Experimenters Guide to the NASA Atmospheric Sciences Research Facility*, Goddard Space Flight Cent., Wallops Flight Facil., Wallops Is., Va., March 1994.
- Stull, R. B., *An Introduction to Boundary Layer Meteorology*, Kluwer Acad., New York, 1998.
- Tatarski, V. I., and M. Charnotskii, On the behavior of scattering from a rough surface for small grazing angles, *IEEE Trans. Antennas Propag.*, 46(1), 67–72, 1998.
- Tarantola, A., *Inverse Problem Theory: Methods for Data Fitting and Model Parameter Estimation*, Elsevier Sci., New York, 1987.
- Toporkov, J. V., R. S. Awadallah, and G. S. Brown, Issues related to the use of a Gaussian-like incident field for low-grazing-angle scattering, *J. Opt. Soc. Am.*, 16, 176–187, 1999.

- Torrungrueng, D., H.-T. Chou, and J. T. Johnson, A novel acceleration algorithm for the computation of scattering from two-dimensional large-scale perfectly conducting random rough surfaces with the forward-backward method, *IEEE Trans. Geosci. Remote Sens.*, 38, 1656–1668, 2000.
- Voronovich, A. G., and V. U. Zavorotny, The effect of steep sea-waves on polarization ratio at low grazing angles, *IEEE Trans. Geosci. Remote Sens.*, 38, 366–373, 2000.
- Wagner, L. J., L. T. Rogers, S. D. Burk, and T. Haack, Island wake impact on evaporation duct height and sea clutter in the lee of Kauai, paper presented at International Geoscience and Remote Sensing Symposium, Sydney, Australia, Int. of Electr. and Electron. Eng., New York, July 2001.
- West, J. C., Integral equation formulation for iterative calculation of scattering from lossy rough surfaces, *IEEE Trans. Geosci. Remote Sens.*, 38, 1609–1615, 2000.
- Wyngaard, J. C., N. L. Seaman, S. J. Kimmel, M. Otte, X. Di, and K. E. Gilbert, Concepts, observations, and simulation of refractive index turbulence in the lower atmosphere, *Radio Sci.*, 36(4), 643–670, 2001.

---

P. Gerstoft and W. S. Hodgkiss, Marine Physical Laboratory, University of California, San Diego, La Jolla, CA 92093-0238, USA. (gerstoft@mpl.ucsd.edu; wsh@mpl.ucsd.edu)

J. L. Krolik, Electrical and Computer Engineering, Duke University, Durham, NC 27708, USA. (jk@ee.duke.edu)

L. T. Rogers, Atmospheric Propagation Branch, SPAWAR Systems Center, San Diego, CA 92152, USA. (trogers@spawar.navy.mil)